Article

# Synergistic Antibacterial Activity of Black Phosphorus Nanosheets Modified with Titanium Aminobenzenesulfanato Complexes

Zhibin Li,[†,‡] Lie Wu,[†] Huaiyu Wang,*[,†] Wenhua Zhou,[†] Hanxia Liu,[†] Haodong Cui,[†] Penghui Li,[†] Paul K. Chu,*[,‡] and Xue-Feng Yu*[,†]

[†]Institute of Biomedicine and Biotechnology, Shenzhen Institutes of Advanced Technology, Chinese Academy of Sciences, Shenzhen 518055, Guangdong, P. R. China

[‡]Department of Physics and Materials Science, City University of Hong Kong, Tat Chee Avenue, Kowloon 999077, Hong Kong, P. R. China

ⓢ Supporting Information

Ti-SA$_4$@BP

Synergistic antibacterial activity
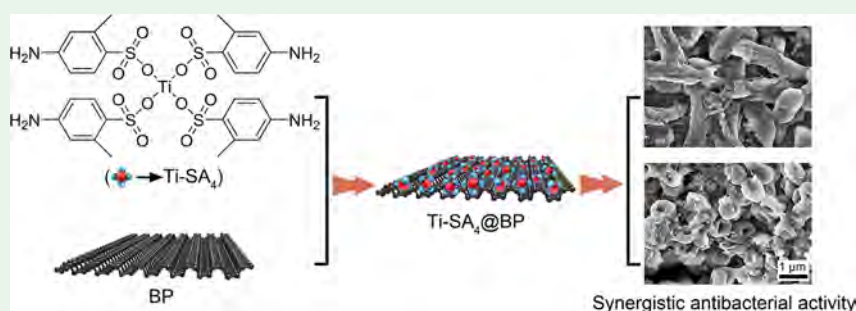
ABSTRACT: A two-dimensional (2D) antimicrobial nanoagent is synthesized by incorporating the titanium amino-benzenesulfanato complexes (Ti-SA$_4$) onto black phosphorus nanosheets (BPs). The strong P−Ti coordination between Ti-SA$_4$ and BPs results in the high loading capacity (∼43%) of Ti-SA$_4$ onto BPs and enhances the stability of BPs against oxidation. Compared to bare BPs and Ti-SA$_4$, the Ti-SA$_4$@BPs exhibit improved antibacterial efficacy, and most of the bacteria are inactivated within 3 h with a dose of only 50 μg/mL. The underlying antibacterial mechanism is investigated. This proposed Ti-SA$_4$@BPs have great potential in clinical applications, and the results provide insights into the design and synthesis of 2D antibacterial nanoagents.

KEYWORDS: *two-dimensional materials, black phosphorus, aminobenzenesulfanato complexes, synergistic antimicrobial activity, surface modification*

1. INTRODUCTION

Infectious diseases caused by pathogenic bacteria pose growing threats to public health.[1] As an alternative to antibiotics, chemotherapeutic sulfa drugs with antimicrobial activity are adopted in clinical treatments, but most of them suffer from low efficiency and severe side effects raised by high-dose administration. In this respect, rapid development of nano-technology in recent years offers the possibility to increase the efficiency of chemical pharmaceuticals.[2−5] Compared with the conventional chemotherapeutic drugs, nanodrugs provide many advantages including limited immunogenicity and cytotoxicity,[6,7] favorable drug release profiles,[8] prolonged circulation, extended half-lives,[9] and targeting ability to specific cells and tissues.[10,11] In particular, ultrathin two-dimensional (2D) nanomaterials[12,13] have elicited increasing interest in biomedicine due to the large surface-to-volume ratio, unique 2D structure with special physicochemical features, and abundance of drug anchoring sites. For example, graphene oxide (GO),[14,15] reduced graphene oxide (rGO),[16−18] and molybdenum disulfide (MoS$_2$)[19−23] have been proposed for drug delivery in cancer therapy due to the high drug loading

capacity.[24,25] In spite of recent progress, the use of 2D materials to deliver antimicrobial drugs is seldom prac-ticed,[26−28] although it has been reported that graphene materials have intrinsically antibacterial activity ascribed to their specific physical effects enabling destructing the bacterial membrane integrity via the extremely sharp edges and/or extracting phospholipids destructively to induce bacterial inactivation.[29,30] However, there are still controversial issues about these antimicrobial effects, and the mechanisms deduced from current achievements are far from exhaustive.[31,32] What is more, most of the 2D materials are not biodegradable naturally,[14,24] thus restricting some clinical applications.

As a new class of 2D nanomaterials, black phosphorus nanosheets (BPs) have aroused increased interest due to their many unique physical and chemical properties. BPs contain only phosphorus, which is an essential element making up about 1% of the total human body weight.[33,34] Furthermore,

BPs are biodegradable and the products are nontoxic phosphate anions.[35,36] Consequently, BPs have recently been used in biomedical applications such as photothermal/ photodynamic therapies,[33,37,38] biosensing,[39] and reinforcing osteoimplants.[40] BPs with the special 2D puckered honeycomb structure have also been employed as a robust platform for loading and delivering anticancer drugs.[41] Nevertheless, the antimicrobial properties and concomitant application of BPs have seldom been reported, perhaps because BPs are quite unstable in the physiological environment,[42] thus complicating drug delivery. Herein, we design and synthesize a novel antimicrobial nanodrug system by loading BPs with titanium aminobenzenesulfanato (designated as Ti-SA$_4$), the well-designed metal complex with antibacterial activity. On account of the strong P−Ti coordination, highly efficient loading of Ti-SA$_4$ onto BPs is achieved, and the as-obtained Ti-SA$_4$@BPs with enhanced stability enable a long-term action. By taking advantage of the synergistic effect of Ti-SA$_4$ and BPs, Ti-SA$_4$@ BPs show a much better antibacterial activity than bare BPs,[43] which can directly deactivated bacteria without the association of near-infrared-mediated photothermal performance.[44,45] Ti-SA$_4$@BPs exhibit a more superior antibacterial activity than Ti-SA$_4$ and BPs, and the underlying synergetic antibacterial mechanism is explored and described.

2. EXPERIMENTAL SECTION

2.1. Materials. 4-Amino-2-methylbenzenesulfonic acid, N-methyl-2-pyrrolidone (NMP), and ethyl alcohol (EtOH) were purchased from Aladdin Reagents (Shanghai, China). Dimethylformamide (DMF) and Ti(O^{i}Pr)$_4$ were obtained from Alfa Aesar (Heysham, UK). Luria-Bertan (LB) broth and LB agar were purchased from Thermo Fisher Scientific (Waltham, MA). The LIVE/DEAD BacLight Bacterial Viability Kit was obtained from Invitrogen (Carlsbad, CA), the genomic DNA extraction kit was obtained from Beyotime (Hangzhou, China), and bulk BP crystals were purchased from MoPhos (China). All the other reagents used in this study were analytical grade, purchased from Sigma-Aldrich (St. Louis, MO), and used directly without further purification. Ultrapure water (Millipore, 18.2 MΩ) was used to prepare the aqueous solutions.

2.2. Synthesis. The BP crystals were dispersed in the NMP solution (25 mL) and treated in an ultrasonic ice bath at 40 kHz frequency. The solution was centrifuged at 4000 rpm for 10 min after exfoliation to remove the unexfoliated bulk, and the supernatant containing the BPs was stored.

To synthesize Ti-SA$_4$, a solution of 4-amino-2-methylbenzene-sulfonic acid in EtOH was added with Ti(O^{i}Pr)$_4$. The molar ratio of 4-amino-2-methylbenzenesulfonic acid to Ti(O^{i}Pr)$_4$ was 4/1. The mixture was heated at 50 °C for 5 h under argon. After removing the solvent, the crude mixture was passed through a bed of silica gel and Ti-SA$_4$ was obtained as a yellow solid.

To fabricate Ti-SA$_4$@BPs, the BPs were dispersed in NMP with the addition of an excessive amount of Ti-SA$_4$. The mixture was stirred in darkness under the protection of Ar environment for 20 h. The mixture was centrifuged at 12000 rpm for 20 min, and the precipitated Ti-SA$_4$@BPs were collected.

2.3. Characterization. ^{1}H NMR and ^{13}C NMR were performed in dimethyl sulfoxide-d_6 (DMSO-d_6) on an Advance DRX Bruker-400 spectrometer at 25 °C. The TEM and HR-TEM images were acquired on a Tecnai G2 F20 S-Twin transmission electron microscope at an acceleration voltage of 200 kV. Raman scattering was conducted on a Horiba Jobin-Yvon Lab Ram HR VIS high-resolution confocal Raman microscope equipped with a 633 nm laser. XPS was conducted on a Thermo Fisher ESCALAB 250Xi XPS. The UV−NIR absorption spectra were acquired at room temperature on a Lambda 25 spectrophotometer (PerkinElmer) with QS-grade quartz cuvettes. The zeta potentials were measured on a zeta potential analyzer (Malvern Instruments Ltd.).

To determine the loading capacity of Ti-SA$_4$, the suspensions of BPs were mixed with Ti-SA$_4$ at different feeding ratios (Ti-SA$_4$/BPs feeding ratios: 0.8, 1.6, 2.4, 3.2, 4, 4.8, 5.6, and 6.4). The loading capacity was measured by inductively coupled plasma atomic emission spectroscopy (ICP-AES). Based on the elemental content of phosphorus and titanium, the loading ratios of Ti-SA$_4$ on BPs were calculated.

2.4. Biocompatibility Assay. The lung microvascular endothelia cells (HULEC-5a) were maintained in red-free endothelial basal medium (Clonetics, San Diego, CA) containing 10% fetal bovine serum (FBS, Invitrogen, Carlsbad, CA), supplemented with 10 ng/mL epidermal growth factor, 1 μg/mL hydrocortisone, 10 mM L-glutamine, 20 IU/mL penicillin, and 20 μg/mL streptomycin. The adenocarcinomic human alveolar basal epithelial cells (A549) were routinely cultured in Dulbecco's Modified Eagle medium (Gibco BRL) supplemented with 10% (v/v) fetal bovine serum. By use of 96-well tissue culture plates as the holders, Ti-SA$_4$@BPs at different concentrations (5, 10, 30, and 50 μg/mL) were incubated with each kind of 1×10^4 cells for 24 h, and the cell viability was determined by a CCK-8 assay (Donjindo) according to the manufacturer's instructions.

2.5. Bacterial Culture. The LB broth was utilized to cultivate the bacteria, and a sterile saline solution was used as a testing medium. The *E. coli* (ATCC 25922) and *S. aureus* (ATCC 43300) were resuspended in 10 mL of LB broth, respectively, and cultivated in a rotating shaker at 37 °C for 12 h. Afterward, 100 μL of the bacterial suspension was transferred to 10 mL of fresh LB broth for subculture and harvested at the exponential growth phase. In the next step, the bacteria were rinsed twice to remove the growth medium constituents and then resuspended in a sterile saline solution (0.9% NaCl). The final bacterial suspension was prepared in a sterile saline solution with a density of 5×10^6 colony-forming units (CFU)/mL.

2.6. LIVE/DEAD Fluorescence Staining. The bacteria viability after different treatments was evaluated by a Live/Dead BacLight kit. The assay was performed according to the manufacturer's instructions. Briefly, 5×10^6 CFU/mL of *E. coli* and *S. aureus* were added with 15 μg/mL Ti-SA$_4$, 35 μg/mL BPs, or 50 μg/mL Ti-SA$_4$@ BPs, and the mixture was incubated under shaking at 200 rpm at 37 °C for 3 h. Subsequently, 1 mL of each specimen was mixed with 2 μL of SYTO 9 and 2 μL of propidium iodide for 15 min incubation in the dark at room temperature. The bacterial solution was centrifuged at 4000 rpm for 5 min and visualized and photographed under a fluorescence microscope (Olympus IX71).

2.7. Antibacterial Assay by Colony Counting. The antibacterial efficacy of the samples was assessed by a colony counting method. The *E. coli* and *S. aureus* (5×10^6 CFU/mL) in 5 mL of the sterile saline solution were incubated with 15 μg/mL Ti-SA$_4$, 35 μg/mL BPs, or 50 μg/mL Ti-SA$_4$@BPs and incubated under shaking at 200 rpm at 37 °C for 3 h. The mixture was diluted with the sterile saline solution and spread on LB agar plates for another 24 h incubation at 37 °C. The viable bacteria were recorded by counting the number of CFU, and the antibacterial ratio was calculated by the formula

$$\text{antibacterial ratio} = (\text{control group CFU} - \text{experimental group CFU})/\text{control group CFU} \times 100\%$$

2.8. SEM Observation of Bacteria Morphology. After incubation with various samples for 3 h, the bacterial suspensions were centrifuged at 4000 rpm for 5 min and rinsed three times with the PBS solution. The bacteria without any treatment were the control. All the bacteria were fixed with a 2.5% glutaraldehyde solution for 2 h, rinsed with PBS three times, and dehydrated with graded ethanol series (30, 50, 70, 80, 90, and 100% v/v) for 10 min. After completely drying at room temperature, the bacteria were sputter-coated with gold (20 s, 30 mA), and the morphology was examined by scanning electron microscopy (Zeiss Sigma 300).

2.9. Zeta Potential and Membrane Potential Assays. After incubation with different samples for 3 h, the bacterial suspensions were centrifuged at 4000 rpm for 5 min and rinsed with the PBS

solution thrice. The zeta potential of treated bacteria was measured on the zeta potential measurement analyzer (Malvern Instruments Ltd.). A BacLight Bacterial Membrane Potential Kit (invitrogen) was used to determine the potential of bacterial membrane. The kit provides a fluorescent membrane potential indicator dye: diethyloxacarbocyanine (DIOC2), which exhibits green fluorescence from all bacteria, but the fluorescence shifts to red when the dye molecules accumulate intracellularly caused by larger membrane potentials. Carbonyl cyanide 3-chlorophenylhydrazone (CCCP) was used as the positive control as it could destroy membrane potential by eradicating the proton gradient. The measurements were performed according to the manufacturer's instructions. Briefly, the bacteria after different treatments were stained with 5 μL of 3 mM DiOC2 in the darkness for 20 min, and the positive control group of bacteria was treated with 10 μL of 500 μM CCCP prior to staining. All the stained bacteria were assayed by Cell Lab Quanta SC flow cytometry (Beckman coulter).

2.10. Bacterial Protein Assay. The proteins extracted from the bacteria were determined by the sodium dodecyl sulfate–polyacrylamide gel electrophoresis (SDS-PAGE) method. The bacteria after different treatments were centrifuged at 4000 rpm for 5 min and rinsed with the PBS solution thrice. The bacteria were then resuspended in a cold lysis buffer (Beyotime, China) supplemented with PMSF at 4 °C for 40 min. The lysates were centrifuged at 4 °C at 14000 rpm for 20 min, and the supernatant extracts were collected. After determining the protein concentration by a BCA assay kit (Beyotime, China), the protein extracts were added with SDS-PAGE loading buffer, heated to 100 °C for 10 min, and separated by 10% SDS-PAGE. The protein gels were stained by Coomassie Brilliant Blue and imaged after water destaining for 12 h.

2.11. DNA Extraction and Fragmentaion Analysis. The bacterial DNA were extracted using a genomic DNA extraction kit according to the manufacturer's instructions. To analyze DNA laddering, the extracted DNA samples of the various experimental groups were separately electrophoresed on a 1% agarose gel containing 0.1% ethidium bromide. The DNA bands were visualized under 312 nm UV radiation.

3. RESULTS AND DISCUSSION

Ti-SA$_4$ is synthesized by a reaction between 4-amino-2-methylbenzenesulfonic acid (SA) and titanium tetraisopropoxide [Ti(O^{i}Pr)$_4$] (Figure 1a). The ^{1}H nuclear magnetic
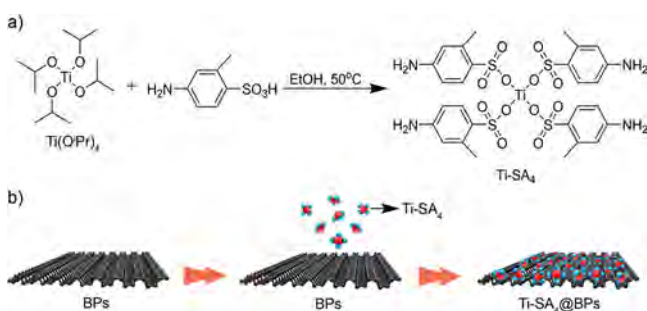

Figure 1. Fabrication of Ti-SA$_4$@BPs: (a) synthesis and structural formula of Ti-SA$_4$; (b) schematic illustration of coordination of Ti-SA$_4$ onto BPs.

resonance (NMR) spectrum of Ti-SA$_4$ (Supporting Information, Figure S1) reveals a singlet at 2.33 ppm attributed to the hydrogen atoms in −CH$_3$, a wide peak at 9.59 ppm ascribed to the hydrogen atoms in −NH$_2$ group, and three multiple peaks at 7.23, 7.30, and 7.60 ppm associated with hydrogen atoms in the benzene ring. The corresponding ^{13}C NMR spectrum (Figure S2) shows the carbon peak in − CH$_3$ at 19.5 ppm, and those at 118.3, 126.8, 127.2, 128.1, 133.4, and 141.3 ppm stem

from carbon atoms in the benzene ring. Both the ^{1}H and ^{13}C NMR spectra confirm successful synthesis of Ti-SA$_4$.

After liquid exfoliation of BPs according to a previously described method,[46] the Ti-SA$_4$@BPs are prepared by loading Ti-SA$_4$ onto BPs via surface coordination (Figure 1b). The samples are characterized by transmission electron microscopy (TEM) and atomic force microscopy (AFM). As shown in Figures 2a and 2b, the Ti-SA$_4$@BPs exhibit the typical 2D morphology with an average lateral size and thickness of ∼220 nm and ∼5 nm, respectively. The high-resolution TEM (HR-TEM) image of Ti-SA$_4$@BPs (inset in Figure 2a) reveals lattice fringes of 2.5 Å corresponding to the (014) plane of BP crystal.

The zeta potentials of BPs before and after Ti-SA$_4$ coordination are shown in Figure 2c. Compared to bare BPs (−31.8 mV), the zeta potential of Ti-SA$_4$@BPs changes to +32.2 mV, which reaches the same level as Ti-SA$_4$ (+28.6 mV). The ^{1}H NMR spectra of Ti-SA$_4$ and Ti-SA$_4$@BPs also exhibit similar results (Figure S1). Both the zeta potentials and ^{1}H NMR data demonstrate successful loading of Ti-SA$_4$ onto BPs. It has been reported that the titanium sulfonate ligand interacts with BPs due to strong P−Ti coordination.[47] Here, the strong electron-withdrawing effect of Ti-SA$_4$ and intrinsic electron-donating property of BPs result in efficient loading of Ti-SA$_4$ onto BPs.

With regard to the characterization by high-resolution X-ray photoelectron spectroscopy (HR-XPS), Ti-SA$_4$@BPs show the typical P 2p$_{3/2}$ (129.5 eV) and P 2p$_{1/2}$ (130.5 eV) doublets of crystalline BP and a broad peak at 132.6 eV corresponding to Ti−P coordination (Figure 2d). The Ti 2p$_{1/2}$ (463.8 eV) and Ti 2p$_{3/2}$ (458.2 eV) peaks are also detected from Ti-SA$_4$@BPs (Figure 2e), in agreement with reported Ti−P coordination.[47] HR-XPS corroborates successful coordination of Ti-SA$_4$ onto BPs. The samples are further examined by Raman scattering (Figure S3). The bare BPs show three typical peaks at 360.0, 437.7, and 466.0 cm^{-1} corresponding to the A$_g^1$, B$_{2g}$, and A$_g^2$ modes of BP.[48] After Ti-SA$_4$ modification, the A$_g^1$, B$_{2g}$, and A$_g^2$ peaks red-shift by about 3.1, 5.2, and 5.4 cm^{-1}, respectively, suggesting that oscillation of P atoms is hindered by Ti−P coordination and the corresponding Raman scattering energy is reduced.[47]

In the next step, the BPs react with Ti-SA$_4$ at an increased feeding ratio of Ti-SA$_4$/BPs, and the obtained Ti-SA$_4$@BPs are analyzed by ICP-AES to determine the loading capacity. As shown in Figure 2f, the loading capacity of Ti-SA$_4$ by BPs shows a typical dose-dependent relationship until a saturation level of about 43% (w/w).

The influence of Ti-SA$_4$ coordination on the stability of BPs is also investigated. As shown in Figure S4, after exposing to the ambient environment, the optical absorption of bare BPs in the aqueous solution decreases gradually, and the solution becomes colorless after 8 days. In contrast, the Ti-SA$_4$@BPs exhibit good stability with well-maintained absorption intensity and solution color during dispersion. The enhanced stability is ascribed to strong P−Ti coordination which occupies the lone electron pair of phosphorus, subsequently preventing BPs from oxidation and facilitating antibacterial applications.

Two common bacteria, *E. coli* (Gram-negative bacterial strain) and *S. aureus* (Gram-postive bacterial strain), are employed to evaluate the antibacterial activity of Ti-SA$_4$@BPs. For comparison, the antibacterial performance of the bare BPs and Ti-SA$_4$ with the same corresponding amount of Ti-SA$_4$@BPs is also studied. 5×10^6 CFU/mL of each bacterial strain is incubated with 15 μg/mL Ti-SA$_4$, 35 μg/mL BPs, or 50 μg/
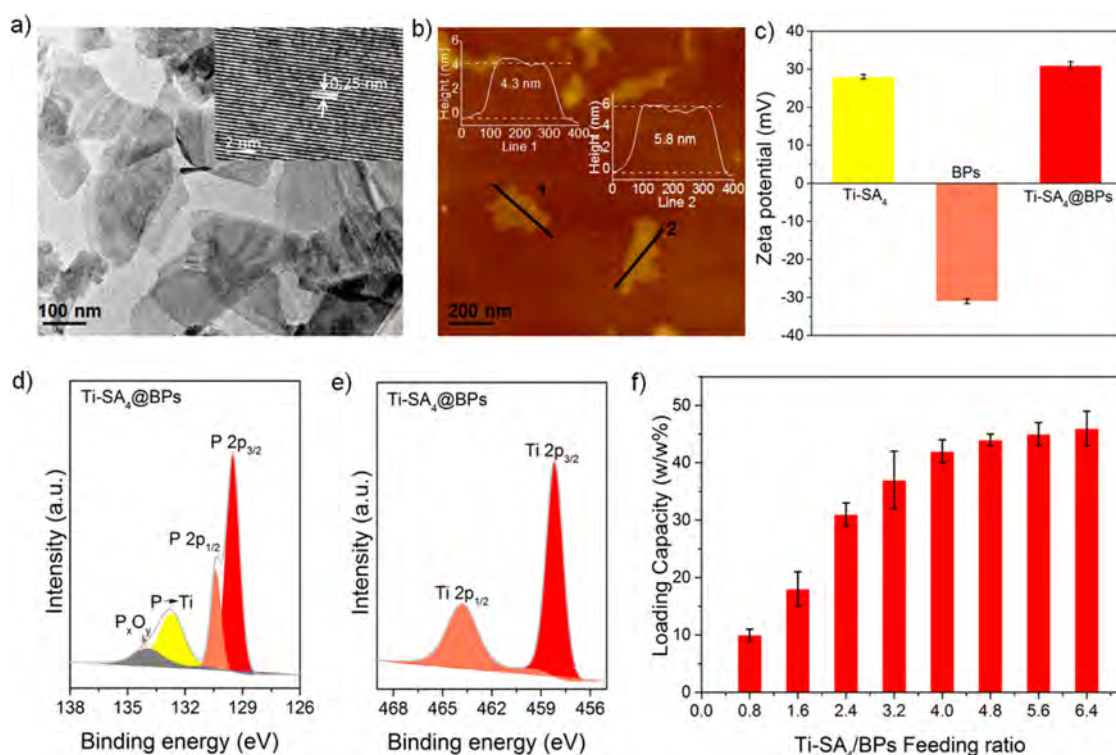
Figure 2. Characterization of Ti-SA$_4$@BPs. (a) TEM image with the inset HR-TEM image of Ti-SA$_4$@BPs. (b) AFM image of Ti-SA$_4$@BPs. The insets show the size and thickness profiles of Ti-SA$_4$@BPs. (c) Zeta potentials of Ti-SA$_4$, BPs, and Ti-SA$_4$@BPs. (d) High-resolution P 2p spectrum of Ti-SA$_4$@BPs. (e) High-resolution Ti 2p spectrum of Ti-SA$_4$@BPs. (f) Loading capacity of Ti-SA$_4$@BPs (w/w%) with increasing feeding ratio of Ti-SA$_4$/BPs.

mL Ti-SA$_4$@BPs and subjected to biological assays. Besides Live/Dead staining, the antibacterial efficacy is quantitatively determined, and the results are displayed in Figure 3. The intense green fluorescence from *E. coli* and *S. aureus* in the blank group indicate that almost all the bacteria are alive. After Ti-SA$_4$ or BPs treatment, green fluorescence recedes, whereas red fluorescence increases, implying that the bacteria are partly sterilized. In comparison, the Ti-SA$_4$@BPs group delivers the most efficient antibacterial performance, from which intense red fluorescence and aggregated dead bacteria are readily observed (Figure 3a). The statistical results determined by colony counting (Figure S5) reveal that sulfonamide Ti-SA$_4$ is insufficient from the perspective of antibacterial efficiency, as only 40.01 ± 3.95% of *E. coli* and 33.55 ± 5.69% of *S. aureus* are inactivated after the Ti-SA$_4$ treatment (Figure 3b). By adopting BPs coordination, the antibacterial ratios of Ti-SA$_4$@BPs go up to 99.23 ± 1.04% (against *E. coli*) and 94.56 ± 2.11% (against *S. aureus*) for the same amount. Moreover, the living bacteria (0.77% for *E. coli* and 5.44% for *S. aureus*) quantities are exponentially smaller than those observed from Ti-SA$_4$ (59.99% for *E. coli* and 66.45% for *S. aureus*) and BPs (84.81% for *E. coli* and 87.69% for *S. aureus*) groups. It is also noted that only an incubation period of 3 h with Ti-SA$_4$@BPs is sufficient to sterilize most of the bacteria (Figure 3c), and the rapid onset of Ti-SA$_4$@BPs is desirable. On the other hand, Ti-SA$_4$@BPs at the same concentration show a good biocompatibility to the mammalian cells (Figure S6) and therefore are very promising in clinical applications.

In view of the outstanding antibacterial properties of Ti-SA$_4$@BPs, the morphological changes of bacteria after different treatments are examined by scanning electron microscopy (SEM). As illustrated in Figure 4, the untreated *E. coli* and *S.*

aureus show the typical bacterial morphology with a smooth surface. With regard to the Ti-SA$_4$ and BPs groups, most of the bacteria retain the normal shape, indicating that the single Ti-SA$_4$ or BPs treatment is not effective enough to produce bacterial membrane damage. In contrast, the bacteria treated by Ti-SA$_4$@BPs are wrinkled, and damaged membranes are observed. The Ti-SA$_4$ ligands designed for this study derive from antimicrobial sulfonamides,[49,50] which are used in clinical treatment of infectious diseases. Nevertheless, similar to most sulfa drugs, Ti-SA$_4$ suffers from low antibacterial efficacy. By combining with BPs coordination, the antibacterial performance of Ti-SA$_4$@BPs is improved significantly compared to Ti-SA$_4$ for the same concentration. The excellent performance stems from strong P–Ti coordination, which leads to local enrichment of Ti-SA$_4$ on the surface of nanosized BPs and subsequently facilitates the interaction between Ti-SA$_4$ and microorganisms to deliver better therapeutic effects. From another point of view, Ti-SA$_4$@BPs with a positive surface potential are much more accessible than bare BPs with negative potential to bacteria with negatively charged membranes.[51] The high affinity between Ti-SA$_4$@BPs and bacteria can effectively isolate the bacteria from the survival condition, and the sharp edges of 2D Ti-SA$_4$@BPs can penetrate the phospholipid membranes of bacteria to destroy the membranes causing eventual bacteria death.[29,52−55]

To investigate the synergistic antibacterial activity of Ti-SA$_4$@BPs and underlying mechanisms, the zeta potentials of bacteria after different treatments are measured. As shown in Figure 5a, both Ti-SA$_4$ and BPs downregulate the negative zeta potential of *E. coli* and *S. aureus*. During incubation with Ti-SA$_4$@BPs, the zeta potential of *E. coli* changes from −14.3 to −2.96 mV and that of *S. aureus* changes from −16.2 to −1.74
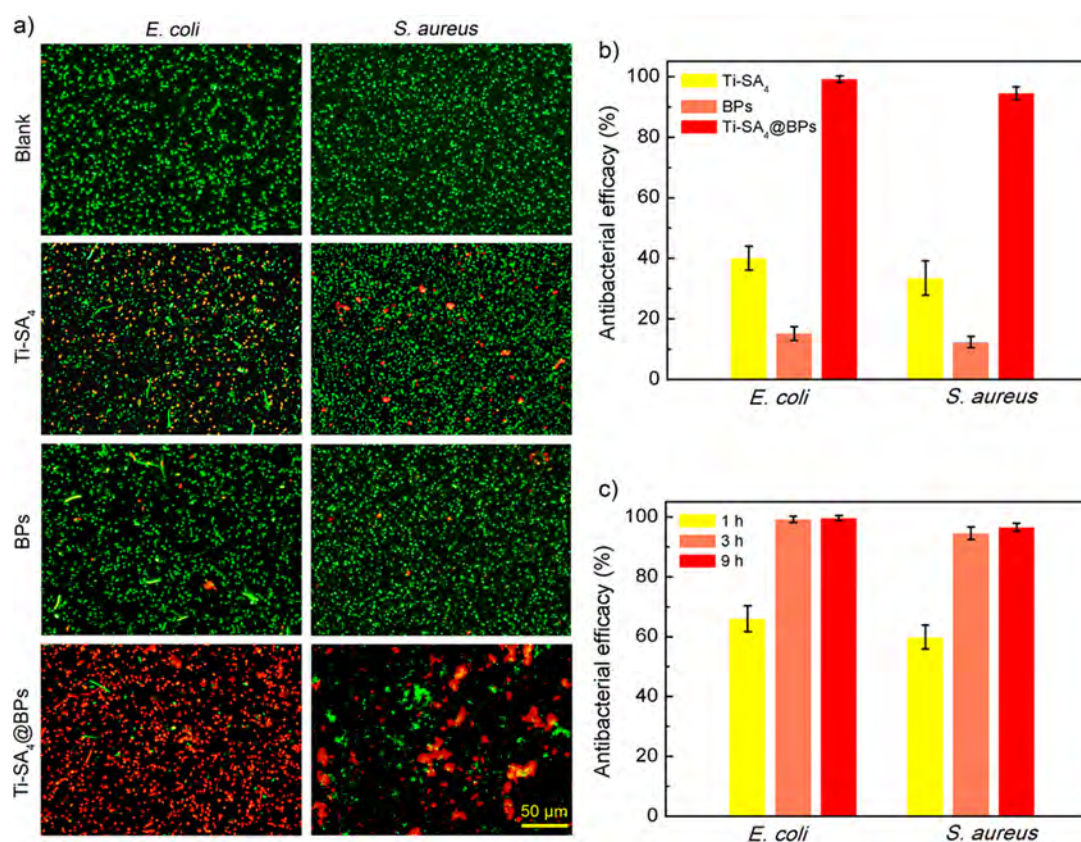
Figure 3. Antibacterial activity against *E. coli* and *S. aureus*. (a) Microscopic images of the different experimental groups after Live/Dead staining. The live bacteria are stained green, and red fluorescence derives from dead microorganisms; the scale bar is valid for all images. (b) Antibacterial efficacy of the different groups. (c) Time-dependent antibacterial efficacy of Ti-SA$_4$@BPs.
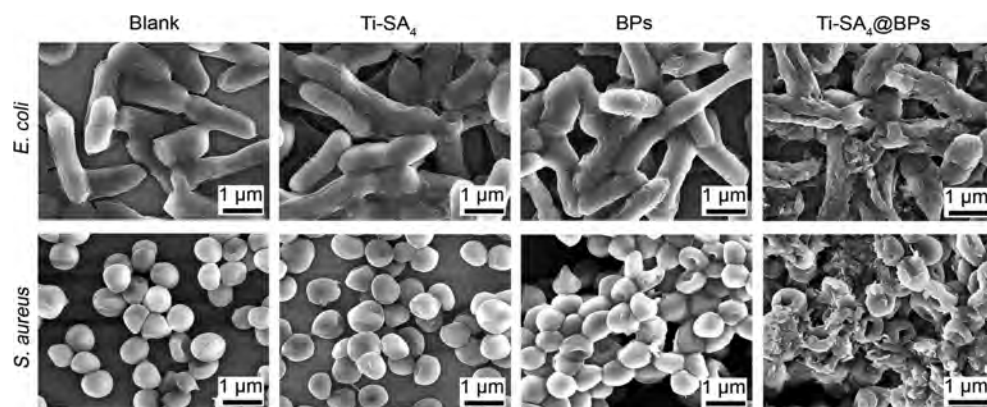

Figure 4. SEM images of *E. coli* and *S. aureus* treated with Ti-SA$_4$, BPs, or Ti-SA$_4$@BPs.

mV. The high affinity between negatively charged bacteria and positively charged Ti-SA$_4$@BPs is corroborated. Actually, the nearly neutral zeta potential values of *E. coli* and *S. aureus* after Ti-SA$_4$@BPs treatment indicate low electrostatic repulsion, which may induce bacterial aggregation and subsequently cause cell death as the results of LIVE/DEAD fluorescence staining shown in Figure 3a. These different groups are further assessed using a BacLight Bacterial Membrane Potential Kit. The carbocyanine dye (3,3′-diethyloxacarbocyanine iodide), which exhibits green fluorescence in all bacterial cells, can shift toward red fluorescence at the higher cytosolic concentrations caused by larger membrane potentials. Therefore, the larger red/green ratio of the stained bacteria is an indicator for the larger membrane potential. As shown in Figure 5b, the bacteria

after the Ti-SA$_4$@BPs treatment show a prominent loss of membrane potential, which is close to the level of the positive control. These results suggest that Ti-SA$_4$@BPs induce bacterial inactivation via a membrane depolarization mechanism. Furthermore, the Ti-SA$_4$@BPs treatment suppresses protein synthesis in the bacteria (Figure 5c, the box with dashed-red border), and the diffused strips of the Ti-SA$_4$@BPs group indicate decomposition of genome DNA (Figure 5d, the box with dashed-red border). The reduced protein synthesis and irreparable DNA damage provide strong evidence about sterilization of bacteria and reveal that Ti-SA$_4$@BPs kill bacteria by destroying the membrane.
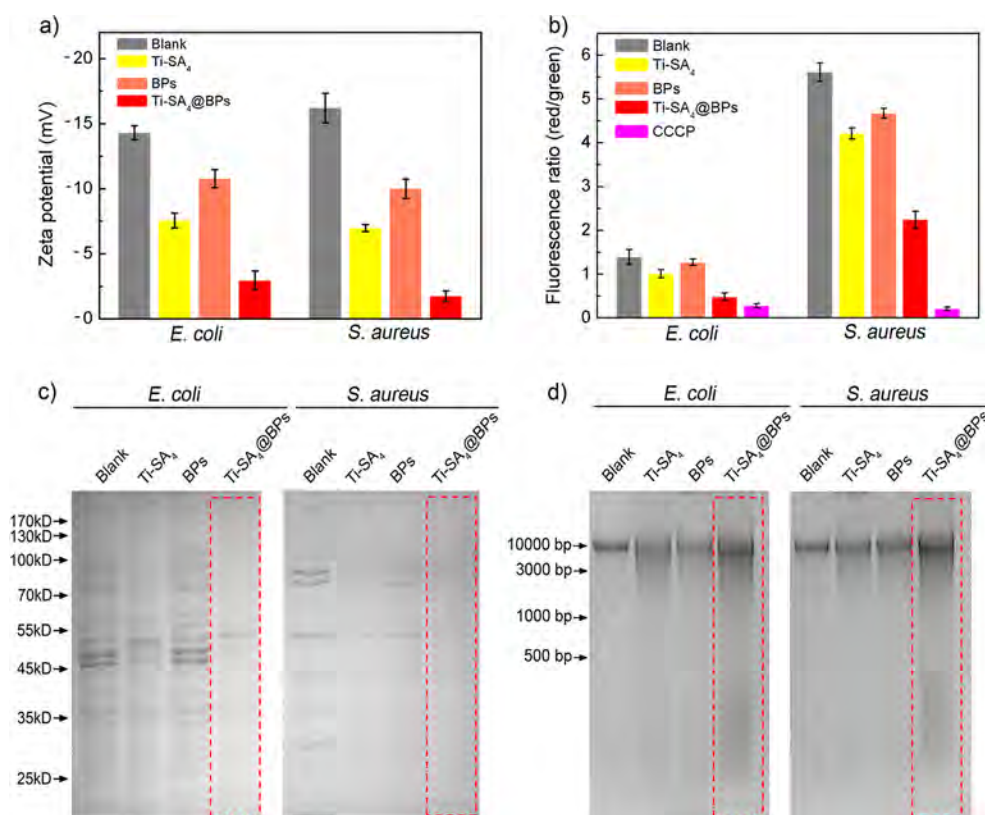
Figure 5. Mechanism of the antibacterial process: (a) zeta potentials of the bacteria after various treatments; (b) assay of bacterial membrane potential; (c) gel electrophoresis analysis of the total bacterial proteins; (d) agarose gel electrophoresis of the bacterial DNA.

4. CONCLUSIONS

In conclusion, a 2D antimicrobial nanoagent is designed and fabricated by loading the titanium aminobenzenesulfanato complexes Ti-SA$_4$ onto BPs. Strong P–Ti coordination gives rise to efficient loading (~43%) of Ti-SA$_4$ onto BPs and enhances the stability of BPs against oxidation. The Ti-SA$_4$@BPs exhibit markedly improved antibacterial efficacy compared to bare Ti-SA$_4$ and BPs. When a dose of about 50 μg/mL is used, the Ti-SA$_4$@BPs are capable of inactivating most of the bacteria within 3 h. Further investigation of the antibacterial mechanism demonstrates that not only the coordination strategy increases the therapeutic effect of Ti-SA$_4$ by locally enriching the antibacterial agents on the surface of nanosized BPs but also the Ti-SA$_4$@BPs with surface positive charges facilitate the interaction with negatively charged bacteria, resulting in the destruction of bacterial membrane, reduced protein synthesis, and irreparable DNA damage. Considering the biodegradability and biocompatibility of BPs, the 2D Ti-SA$_4$@BPs are promising in clinical applications. Furthermore, the results provide insights into the design and synthesis of new 2D nanoagents that can meet the multifarious and rigorous requirements of biomedicine.

ASSOCIATED CONTENT

Ⓢ Supporting Information

The Supporting Information is available free of charge on the ACS Publications Web site at DOI: The Supporting Information is available free of charge on the ACS Publications website at DOI: 10.1021/acsanm.8b02065.

Additional characterizations including ¹H NMR spectra, ¹³C NMR spectra, and Raman scattering spectra; additional figures including sample stability, bacterial colonies, and biocompatibility assay (PDF)

AUTHOR INFORMATION

Corresponding Authors
*E-mail: xf.yu@siat.ac.cn (X.-F.Y.).
*E-mail: hy.wang1@siat.ac.cn (H.Y.W.).
*E-mail: paul.chu@cityu.edu.hk (P.K.C.).

ORCID Ⓘ
Huaiyu Wang: 0000-0002-7189-9944
Penghui Li: 0000-0001-7257-6381
Xue-Feng Yu: 0000-0003-2566-6194

Author Contributions
Z.B.L. and L.W. contributed equally to this work.

Notes
The authors declare no competing financial interest.

■ REFERENCES

(1) Jones, K. E.; Patel, N. G.; Levy, M. A.; Storeygard, A.; Balk, D.; Gittleman, J. L.; Daszak, P. Global Trends in Emerging Infectious Diseases. *Nature* **2008**, *451*, 990−993.

(2) Pelgrift, R. Y.; Friedman, A. J. Nanotechnology as a Therapeutic Tool to Combat Microbial Resistance. *Adv. Drug Delivery Rev.* **2013**, *65*, 1803−1815.

(3) Wang, L.; Hu, C.; Shao, L. The Antimicrobial Activity of Nanoparticles: Present Situation and Prospects for the Future. *Int. J. Nanomed.* **2017**, *12*, 1227−1249.

(4) Hemeg, H. A. Nanomaterials for Alternative Antibacterial Therapy. *Int. J. Nanomed.* **2017**, *12*, 8211−8225.

(5) Alvarez-Paino, M.; Muñoz-Bonilla, A.; Fernández-García, M. Antimicrobial Polymers in The Nano-World. *Nanomaterials* **2017**, *7*, 48.

(6) Pelaz, B.; Alexiou, C.; Alvarez-Puebla, R. A.; Alves, F.; Andrews, A. M.; Ashraf, S.; Balogh, L. P.; Ballerini, L.; Bestetti, A.; Brendel, C.; Bosi, S.; Carril, M.; Chan, W. C.; Chen, C.; Chen, X.; Cheng, Z.; Cui, D.; Du, J.; Dullin, C.; Escudero, A.; Feliu, N.; Gao, M.; George, M.; Gogotsi, Y.; Grünweller, A.; Gu, Z.; Halas, N. J.; Hampp, N.; Hartmann, R. K.; Hersam, M. C.; Hunziker, P.; Jian, J.; Jiang, X.; Jungebluth, P.; Kataoka, K.; Khademhosseini, A.; Kopeček, J.; Kotov, N. A.; Krug, H. F.; Lee, D. S.; Lehr, C. M.; Leong, K. W.; Liang, X. J.; Ling, Lim. M.; Liz-Marzán, L. M.; Ma, X.; Macchiarini, P.; Meng, H.; Möhwald, H.; Mulvaney, P.; Nel, A. E.; Nie, S.; Nordlander, P.; Okano, T.; Oliveira, J.; Park, T. H.; Penner, R. M.; Prato, M.; Puntes, V.; Rotello, V. M.; Samarakoon, A.; Schaak, R. E.; Shen, Y.; Sjöqvist, S.; Skirtach, A. G.; Soliman, M. G.; Stevens, M. M.; Sung, H. W.; Tang, B. Z.; Tietze, R.; Udugama, B. N.; VanEpps, J. S.; Weil, T.; Weiss, P. S.; Willner, I.; Wu, Y.; Yang, L.; Yue, Z.; Zhang, Q.; Zhang, Q.; Zhang, X. E.; Zhao, Y.; Zhou, X.; Parak, W. J. Diverse Applications of Nanomedicine. *ACS Nano* **2017**, *11*, 2313−2381.

(7) Bourzac, K. Nanotechnology: Carrying drugs. *Nature* **2012**, *491*, S58−S60.

(8) Tran, S.; DeGiovanni, P. J.; Piel, B.; Rai, P. Cancer Nanomedicine: A Review of Recent Success in Drug Delivery. *Clin. Transl. Med.* **2017**, *6*, 1−21.

(9) Timin, A. S.; Litvak, M. M.; Gorin, D. A.; Atochina-Vasserman, E. N.; Atochin, D. N.; Sukhorukov, G. B. Cell-Based Drug Delivery and Use of Nano-and Microcarriers for Cell Functionalization. *Adv. Healthcare Mater.* **2018**, *7*, 1870012.

(10) Chen, T.; Shukoor, M. I.; Wang, R.; Zhao, Z.; Yuan, Q.; Bamrungsap, S.; Xiong, X.; Tan, W. Smart Multifunctional Nanostructure for Targeted Cancer Chemotherapy and Magnetic Resonance Imaging. *ACS Nano* **2011**, *5*, 7866−7873.

(11) Peer, D.; Karp, J. M.; Hong, S.; Farokhzad, O. C.; Margalit, R.; Langer, R. Nanocarriers as An Emerging Platform for Cancer Therapy. *Nat. Nanotechnol.* **2007**, *2*, 751−760.

(12) Zhang, H. Ultrathin Two-Dimensional Nanomaterials. *ACS Nano* **2015**, *9*, 9451−9469.

(13) Tan, C.; Cao, X.; Wu, X. J.; He, Q.; Yang, J.; Zhang, X.; Chen, J.; Zhao, W.; Han, S.; Nam, G. H.; Sindoro, M.; Zhang, H. Recent Advances in Ultrathin Two-Dimensional Nanomaterials. *Chem. Rev.* **2017**, *117*, 6225−6331.

(14) Mao, H. Y.; Laurent, S.; Chen, W.; Akhavan, O.; Imani, M.; Ashkarran, A. A.; Mahmoudi, M. Graphene: Promises, Facts, Opportunities, and Challenges in Nanomedicine. *Chem. Rev.* **2013**, *113*, 3407−3424.

(15) Nejabat, M.; Charbgoo, F.; Ramezani, M. Graphene as Multifunctional Delivery Platform in Cancer Therapy. *J. Biomed. Mater. Res., Part A* **2017**, *105*, 2355−2367.

(16) Li, Y.; Lu, Q.; Liu, H.; Wang, J.; Zhang, P.; Liang, H.; Jiang, L.; Wang, S. Antibody-Modified Reduced Graphene Oxide Films with Extreme Sensitivity to Circulating Tumor Cells. *Adv. Mater.* **2015**, *27*, 6848−6854.

(17) Cheon, Y. A.; Bae, J. H.; Chung, B. G. Reduced Graphene Oxide Nanosheet for Chemo-Photothermal Therapy. *Langmuir* **2016**, *32*, 2731−2736.

(18) Miao, W.; Shim, G.; Kang, C. M.; Lee, S.; Choe, Y. S.; Choi, H. G.; Oh, Y. K. Cholesteryl Hyaluronic Acid-Coated, Reduced Graphene Oxide Nanosheets For Anti-Cancer Drug Delivery. *Biomaterials* **2013**, *34*, 9638−9647.

(19) Chou, S. S.; Kaehr, B.; Kim, J.; Foley, B. M.; De, M.; Hopkins, P. E.; Huang, J.; Brinker, C. J.; Dravid, V. P. Chemically Exfoliated MoS$_2$ as Near-Infrared Photothermal Agents. *Angew. Chem., Int. Ed.* **2013**, *52*, 4160−4164.

(20) Peng, M. Y.; Zheng, D. W.; Wang, S. B.; Cheng, S. X.; Zhang, X. Z. Multifunctional Nanosystem for Synergistic Tumor Therapy Delivered by Two-Dimensional MoS$_2$. *ACS Appl. Mater. Interfaces* **2017**, *9*, 13965−13975.

(21) Liu, T.; Shi, S.; Liang, C.; Shen, S.; Cheng, L.; Wang, C.; Song, X.; Goel, S.; Barnhart, T. E.; Cai, W.; Liu, Z. Iron Oxide Decorated MoS$_2$ Nanosheets With Double PEGylation for Chelator-Free Radiolabeling and Multimodal Imaging Guided Photothermal Therapy. *ACS Nano* **2015**, *9*, 950−960.

(22) Kong, L.; Xing, L.; Zhou, B.; Du, L.; Shi, X. Dendrimer-Modified MoS$_2$ Nanoflakes as a Platform for Combinational Gene Silencing and Photothermal Therapy of Tumors. *ACS Appl. Mater. Interfaces* **2017**, *9*, 15995−16005.

(23) Chen, L.; Zhou, X.; Nie, W.; Feng, W.; Zhang, Q.; Wang, W.; Zhang, Y.; Chen, Z.; Huang, P.; He, C. Marriage of Albumin-Gadolinium Complexes and MoS$_2$ Nanoflakes as Cancer Theranostics for Dual-Modality Magnetic Resonance/Photoacoustic Imaging and Photothermal Therapy. *ACS Appl. Mater. Interfaces* **2017**, *9*, 17786−17798.

(24) Kurapati, R.; Kostarelos, K.; Prato, M.; Bianco, A. Biomedical Uses for 2D Materials Beyond Graphene: Current Advances and Challenges Ahead. *Adv. Mater.* **2016**, *28*, 6052−6074.

(25) Chen, W.; Ouyang, J.; Liu, H.; Chen, M.; Zeng, K.; Sheng, J.; Liu, Z.; Han, Y.; Wang, L.; Li, J.; Deng, L.; Liu, Y.; Guo, S. Black Phosphorus Nanosheet-Based Drug Delivery System For Synergistic Photodynamic/Photothermal/Chemotherapy of Cancer. *Adv. Mater.* **2017**, *29*, 1603864.

(26) Zhang, X.; Zhang, W.; Liu, L.; Yang, M.; Huang, L.; Chen, K.; Wang, R.; Yang, B.; Zhang, D.; Wang, J. Antibiotic-loaded MoS$_2$ Nanosheets to Combat Bacterial Resistance via Biofilm Inhibition. *Nanotechnology* **2017**, *28*, 225101.

(27) Pandey, H.; Parashar, V.; Parashar, R.; Prakash, R.; Ramteke, P. W.; Pandey, A. C. Controlled Drug Release Characteristics and Enhanced Antibacterial Effect of Graphene Nanosheets Containing Gentamicin Sulfate. *Nanoscale* **2011**, *3*, 4104−4108.

(28) Mejías Carpio, I. E.; Santos, C. M.; Wei, X.; Rodrigues, D. F. Toxicity of a Polymer−Graphene Oxide Composite Against Bacterial Planktonic Cells, Biofilms, and Mammalian Cells. *Nanoscale* **2012**, *4*, 4746−4756.

(29) Zou, X.; Zhang, L.; Wang, Z.; Luo, Y. Mechanisms of the Antimicrobial Activities of Graphene Materials. *J. Am. Chem. Soc.* **2016**, *138*, 2064−2077.

(30) Tu, Y.; Lv, M.; Xiu, P.; Huynh, T.; Zhang, M.; Castelli, M.; Liu, Z.; Huang, Q.; Fan, C.; Fang, H.; Zhou, R. Destructive Extraction of Phospholipids from *Escherichia coli* Membranes by Graphene Nanosheets. *Nat. Nanotechnol.* **2013**, *8*, 594−601.

(31) Hui, L.; Piao, J. G.; Auletta, J.; Hu, K.; Zhu, Y.; Meyer, T.; Liu, H.; Yang, L. Availability of the Basal Planes of Graphene Oxide Determines Whether It is Antibacterial. *ACS Appl. Mater. Interfaces* **2014**, *6*, 13183−13190.

(32) Luo, Y.; Yang, X.; Tan, X.; Xu, L.; Liu, Z.; Xiao, J.; Peng, R. Functionalized Graphene Oxide in Microbial Engineering: an Effective Stimulator for Bacterial Growth. *Carbon* **2016**, *103*, 172−180.

(33) Yi, Y.; Yu, X. F.; Zhou, W.; Wang, J.; Chu, P. K. Two-Dimensional Black Phosphorus: Synthesis, Modification, Properties, and Applications. *Mater. Sci. Eng., R* **2017**, *120*, 1−33.

(34) Wang, H.; Yu, X. F. Few-Layered Black Phosphorus: From Fabrication and Customization to Biomedical Applications. *Small* **2018**, *14*, 1702830.

(35) Shao, J.; Xie, H.; Huang, H.; Li, Z.; Sun, Z.; Xu, Y.; Xiao, Q.; Yu, X. F.; Zhao, Y.; Zhang, H.; Wang, H.; Chu, P. K. Biodegradable Black Phosphorus-Based Nanospheres for *in Vivo* Photothermal Cancer Therapy. *Nat. Commun.* **2016**, *7*, 1−13.

(36) Sun, Z.; Xie, H.; Tang, S.; Yu, X. F.; Guo, Z.; Shao, J.; Zhang, H.; Huang, H.; Wang, H.; Chu, P. K. Ultrasmall Black Phosphorus Quantum Dots: Synthesis and Use as Photothermal Agents. *Angew. Chem., Int. Ed.* **2015**, *54*, 11526−11530.

(37) Yang, X.; Liu, G.; Shi, Y.; Huang, W.; SHAO, J.; Dong, X. Nano-Black Phosphorus for Combined Cancer Phototherapy: Recent Advances and Prospects. *Nanotechnology* **2018**, *29*, 222001.

(38) Choi, J. R.; Yong, K. W.; Choi, J. Y.; Nilghaz, A.; Lin, Y.; Xu, J.; Lu, X. Black Phosphorus and Its Biomedical Applications. *Theranostics* **2018**, *8*, 1005−1026.

(39) Chen, Y.; Ren, R.; Pu, H.; Chang, J.; Mao, S.; Chen, J. Field-Effect Transistor Biosensors with Two-Dimensional Black Phosphorus Nanosheets. *Biosens. Bioelectron.* **2017**, *89*, 505−510.

(40) Yang, B.; Yin, J.; Chen, Y.; Pan, S.; Yao, H.; Gao, Y.; Shi, J. 2D-Black-Phosphorus-Reinforced 3D-Printed Scaffolds: A Stepwise Countermeasure for Osteosarcoma. *Adv. Mater.* **2018**, *30*, 1705611.

(41) Tao, W.; Zhu, X.; Yu, X.; Zeng, X.; Xiao, Q.; Zhang, X.; Ji, X.; Wang, X.; Shi, J.; Zhang, H.; Mei, L. Black Phosphorus Nanosheets as A Robust Delivery Platform for Cancer Theranostics. *Adv. Mater.* **2017**, *29*, 1.

(42) Huang, Y.; Qiao, J.; He, K.; Bliznakov, S.; Sutter, E.; Chen, X.; Luo, D.; Meng, F.; Su, D.; Decker, J.; Ji, W.; Ruoff, R.; Sutter, P. Interaction of Black Phosphorus with Oxygen and Water. *Chem. Mater.* **2016**, *28*, 8330−8339.

(43) Xiong, Z.; Zhang, X.; Zhang, S.; Lei, L.; Ma, W.; Li, D.; Wang, W.; Zhao, Q.; Xing, B. Bacterial Toxicity of Exfoliated Black Phosphorus Nanosheets. *Ecotoxicol. Environ. Saf.* **2018**, *161*, 507−514.

(44) Sun, Z.; Zhang, Y.; Yu, H.; Yan, C.; Liu, Y.; Hong, S.; Tao, H.; Robertson, A. W.; Wang, Z.; Pádua, A. A. H. New Solvent-Stabilized Few-Layer Black Phosphorus for Antibacterial Applications. *Nanoscale* **2018**, *10*, 12543−12553.

(45) Ouyang, J.; Liu, R. Y.; Chen, W. S.; Liu, Z. J.; Xu, Q. F.; Zeng, K.; Deng, L.; Shen, L. F.; Liu, Y. N. A Black Phosphorus Based Synergistic Antibacterial Platform Against Drug Resistant Bacteria. *J. Mater. Chem. B* **2018**, *6*, 6302−6310.

(46) Guo, Z.; Zhang, H.; Lu, S.; Wang, Z.; Tang, S.; Shao, J.; Sun, Z.; Xie, H.; Wang, H.; Yu, X. F.; Chu, P. K. From Black Phosphorus to Phosphorene: Basic Solvent Exfoliation, Evolution of Raman Scattering, and Applications to Ultrafast Photonics. *Adv. Funct. Mater.* **2015**, *25*, 6996−7002.

(47) Zhao, Y.; Wang, H.; Huang, H.; Xiao, Q.; Xu, Y.; Guo, Z.; Xie, H.; Shao, J.; Sun, Z.; Han, W.; Yu, X. F.; Li, P.; Chu, P. K. Surface Coordination of Black Phosphorus for Robust Air and Water Stability. *Angew. Chem., Int. Ed.* **2016**, *55*, 5003−5007.

(48) Zhao, Y.; Tong, L.; Li, Z.; Yang, N.; Fu, H.; Wu, L.; Cui, H.; Zhou, W.; Wang, J.; Wang, H.; Chu, P. K.; Yu, X. F. Stable and Multifunctional Dye-Modified Black Phosphorus Nanosheets for Near-Infrared Imaging-Guided Photothermal Therapy. *Chem. Mater.* **2017**, *29*, 7131−7139.

(49) Wulf, N. R.; Matuszewski, K. A. Sulfonamide Cross-Reactivity: Is There Evidence to Support Broad Cross-Allergenicity? *Am. J. Health-Syst. Pharm.* **2013**, *70*, 1483−1494.

(50) Ibrahim, H. S.; Eldehna, W. M.; Abdel-Aziz, H. A.; Elaasser, M. M.; Abdel-Aziz, M. M. Improvement of Antibacterial Activity of Some Sulfa Drugs through Linkage to Certain Phthalazin-1(2H)-one Scaffolds. *Eur. J. Med. Chem.* **2014**, *85*, 480−486.

(51) Gottenbos, B.; Grijpma, D. W.; van der Mei, H. C.; Feijen, J.; Busscher, H. J. Antimicrobial Effects of Positively Charged Surfaces on Adhering Gram-Positive and Gram-Negative Bacteria. *J. Antimicrob. Chemother.* **2001**, *48*, 7−13.

(52) Akhavan, O.; Ghaderi, E. Toxicity of Graphene and Graphene Oxide Nanowalls Against Bacteria. *ACS Nano* **2010**, *4*, 5731−5736.

(53) Pham, V. T. H.; Truong, V. K.; Quinn, M. D. J.; Notley, S. M.; Guo, Y.; Baulin, V. A.; Al Kobaisi, M.; Crawford, R. J.; Ivanova, E. P. Graphene Induces Formation of Pores that Kill Spherical and Rod-Shaped Bacteria. *ACS Nano* **2015**, *9*, 8458−8467.

(54) Li, Y.; Yuan, H.; von dem Bussche, A.; Creighton, M.; Hurt, R. H.; Kane, A. B.; Gao, H. Graphene Microsheets Enter Cells Through Spontaneous Membrane Penetration at Edge Asperities and Corner Sites. *Proc. Natl. Acad. Sci. U. S. A.* **2013**, *110*, 12295−12300.

(55) Prasad, K.; Lekshmi, G. S.; Ostrikov, K.; Lussini, V.; Blinco, J.; Mohandas, M.; Vasilev, K.; Bottle, S.; Bazaka, K.; Ostrikov, K. Synergic Bactericidal Effects of Reduced Graphene Oxide and Silver Nanoparticles Against Gram-Positive and Gram-Negative Bacteria. *Sci. Rep.* **2017**, *7*, 1−11.

Supporting Information

Synergistic Antibacterial Activity of Black Phosphorus Nanosheets Modified with Titanium Aminobenzenesulfanato Complexes

Zhibin Li,[†,‡,#] Lie Wu,[†,#] Huaiyu Wang,[†,*] Wenhua Zhou,[†] Hanxia Liu,[†] Haodong Cui,[†]

Penghui Li,[†] Paul K. Chu,[‡,*] and Xue-Feng Yu[†,*]

[†] Institute of Biomedicine and Biotechnology, Shenzhen Institutes of Advanced Technology, Chinese Academy of Sciences, Shenzhen 518055, Guangdong, P. R. China

[‡] Department of Physics and Materials Science, City University of Hong Kong, Tat Chee Avenue, Kowloon 999077, Hong Kong, China

KEYWORDS: two-dimentional materials, black phosphorus, aminobenzenesulfanato complexes, synergistic antimicrobial activity, surface modification

Corresponding Authors:

*E-mail: xf.yu@siat.ac.cn (X. -F. Yu); hy.wang1@siat.ac.cn (H. Y. Wang);

paul.chu@cityu.edu.hk (P. K. Chu)
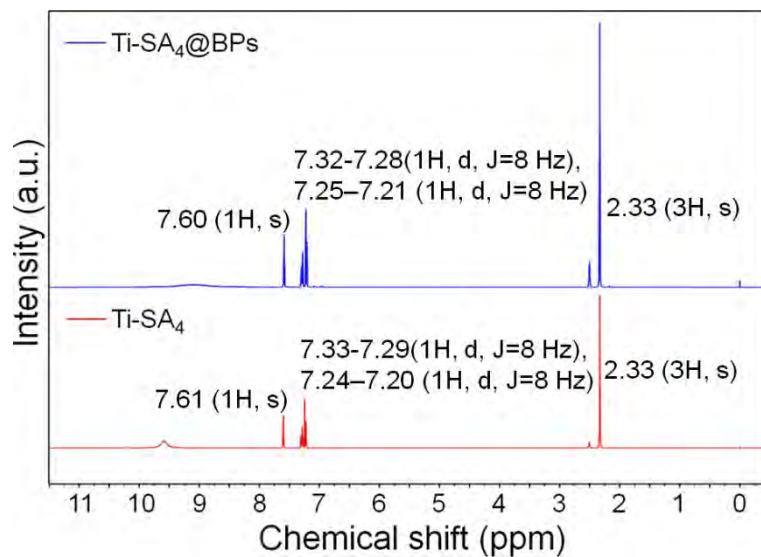
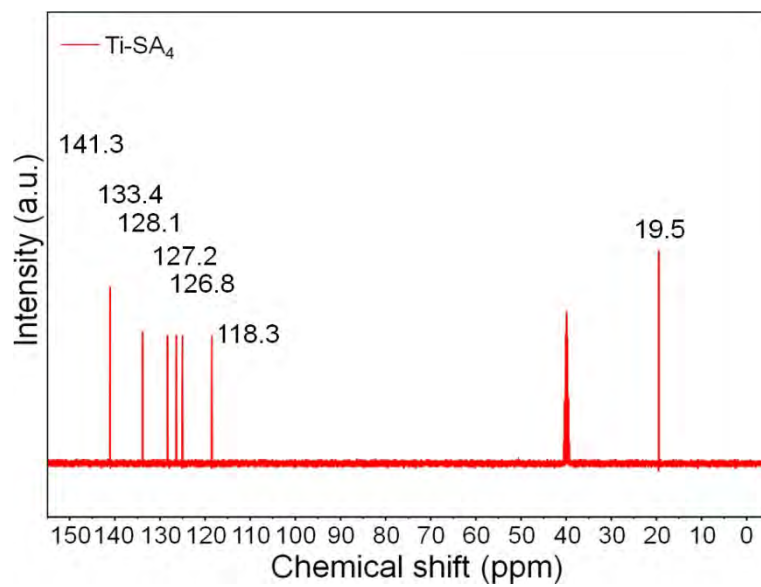**Figure S1.** The ^{1}H NMR spectra of Ti-SA$_4$ and Ti-SA$_4$@BPs.

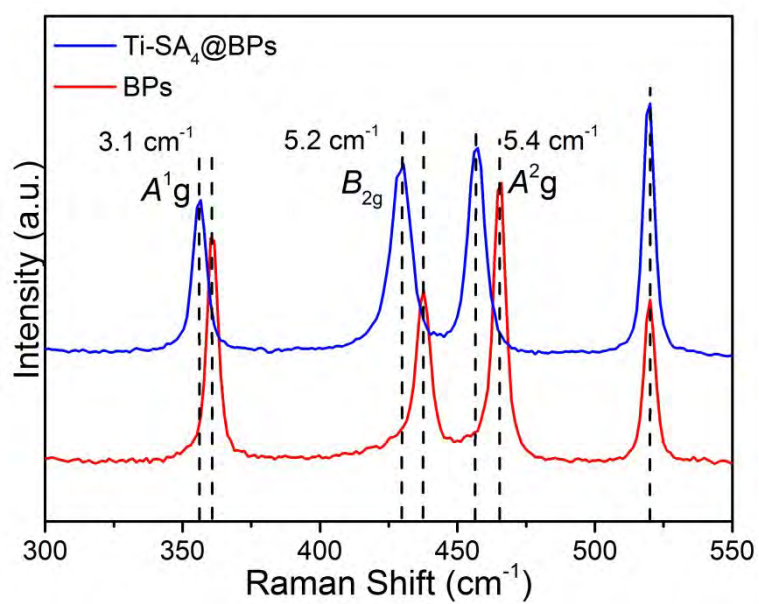**Figure S2.** The ^{13}C NMR spectra of Ti-SA$_4$.

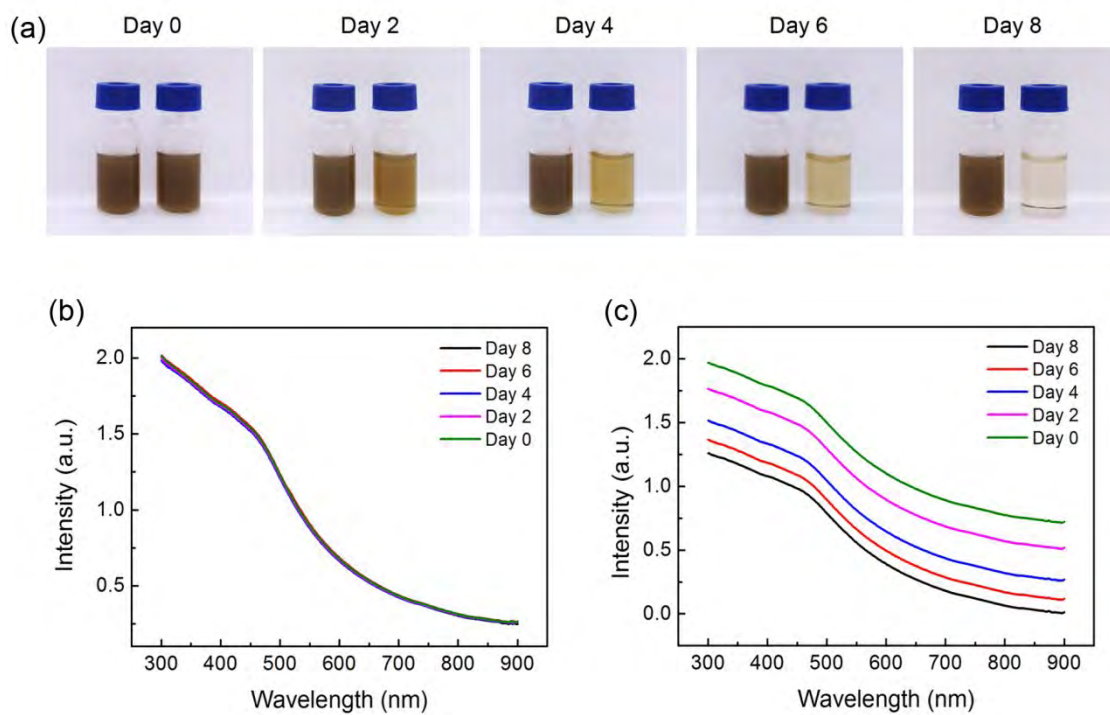**Figure S3.** Raman scattering spectra of bare BPs and Ti-SA$_4$@BPs.

Figure S4. Stability of Ti-SA$_4$@BPs and bare BPs resuspended in pure water: (a) Photographs and time-dependent absorption spectra of (b) Ti-SA$_4$@BPs and (c) Bare BPs at an initial concentration of 100 μg/mL.
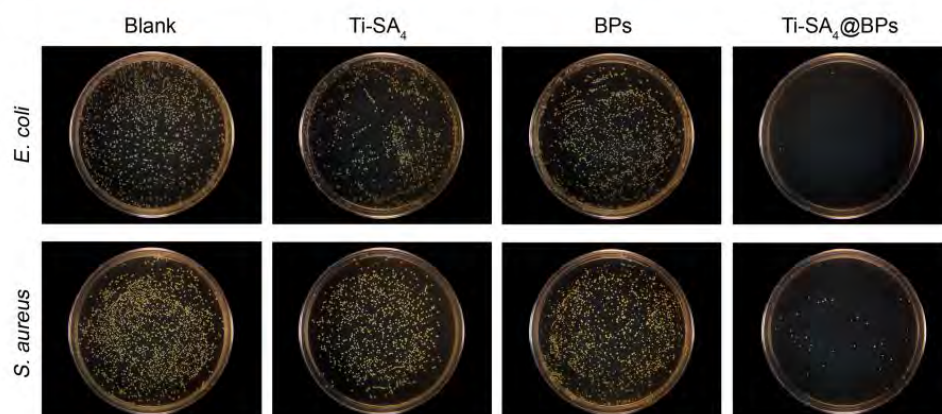
Figure S5. Images of the bacterial colonies after different treatments for 3 h.
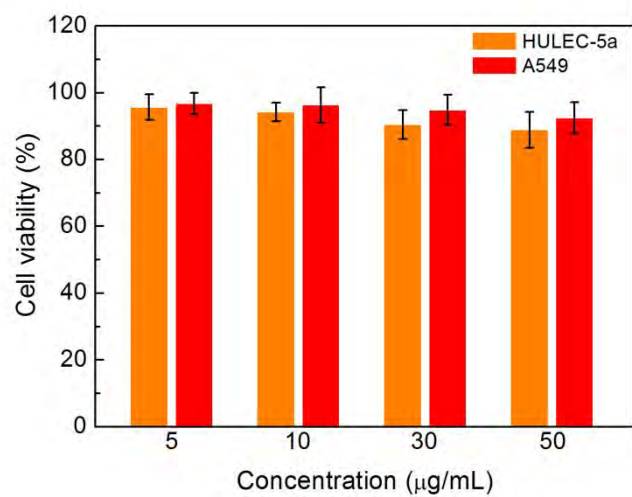
Figure S6. Cell viability of HULEC-5a and A549 cells after the treatments with different concentrations of Ti-SA$_4$@BPs for 24 h.